Contents lists available at ScienceDirect

Transactions of Nonferrous Metals Society of China

36(2026) 917−928

www.tnmsc.cn

Magnetic hardening strategy for high-performance Sm(CoFeCuZr)$_z$ sintered permanent magnets prepared by dual-alloy process

Jian-jun YANG [a,b], Dong-tao ZHANG [a,c,*], Yu-qing LI [a,c], Zan LONG [a,c], Cheng-zhen MENG [a,c], Wei-qiang LIU [a,c], Ming YUE [a,c,**]

[a] Key Laboratory of Advanced Functional Materials, Ministry of Education, College of Materials Science and Engineering, Beijing University of Technology, Beijing 100124, China;

[b] School of Mechanical and Aerospace Manufacturing Engineering, Anyang Institute of Technology, Anyang 455000, China;

[c] State Key Laboratory of Materials Low-Carbon Recycling, Beijing University of Technology, Beijing 100124, China

---

Abstract: To improve the overall magnetic properties of Sm(CoFeCuZr)$_z$ sintered magnets, a dual-alloy sintering process that involves mixing high-iron, low-copper powders with low-iron, high-copper powders was systematically investigated. The results demonstrate that this method significantly improves the Cu-lean phenomenon at the grain boundaries, achieves multiscale uniform microstructures, greatly enhances the pinning field strength, and ultimately produces a high-performance dual-alloy magnet with a maximum energy product ($(BH)_{\max}$) exceeding 240 kJ/m^3 and an intrinsic coercivity (H_{cj}) exceeding 2400 kA/m. In particular, when 35 wt.% of low-iron, high-copper alloy powder is incorporated, the dual-alloy magnet achieves a remanence of 1.13 T, H_{cj} of 2691.2 kA/m and $(BH)_{\max}$ of 248 kJ/m^3. To evaluate the overall magnetic performance, the sum of H_{cj} (in kA/m) and $(BH)_{\max}$ (in kJ/m^3) is used as a combined parameter, yielding a value of 2939.2. Compared with single-alloy magnets of the same composition, the dual-alloy sintering process yields magnets with a more uniform elemental distribution and superior magnetic properties.

Keywords: Sm(CoFeCuZr)$_z$ magnets; dual-alloy sintering process; magnetic properties; coercivity mechanism; magnetisation reversal process

---

1 Introduction

Sm(CoFeCuZr)$_z$ magnets have rapidly emerged as the preferred choice for high-temperature permanent magnets and promising candidates for designing high-performance nanocomposite magnets compared to Nd−Fe−B magnets [1], owing to their outstanding intrinsic magnetic properties, exceptional temperature stability and excellent corrosion resistance [2−4]. Recently, rapid advancements in high-tech industries such as aerospace, 5G communication, advanced rail transportation and high-power permanent magnet motors have driven the demand for improved magnetic properties in Sm(CoFeCuZr)$_z$ sintered magnets. Commercial 2:17-type Sm−Co magnets typically operate at temperatures below 350 °C. However, at elevated temperatures (above 350 °C), Sm(CoFeCuZr)$_z$ sintered magnets experience a considerable reduction in the maximum energy product $(BH)_{\max}$, knee coercivity (H_{k}) and intrinsic coercivity (H_{cj}) [5]. To expand the operational temperature range of these magnets, enhancing their overall magnetic performance (OMP) is crucial. Specifically, $(BH)_{\max}$ should exceed 240 kJ/m^3 and

---

Corresponding author: *Dong-tao ZHANG, Tel: +86-10-67391760, E-mail: zdt@bjut.edu.cn;
**Ming YUE, Tel: +86-10-67391760, E-mail: yueming@bjut.edu.cn

https://doi.org/10.1016/S1003-6326(25)67006-3
Received 4 July 2024; accepted 18 April 2025

H_{cj} should exceed 2400 kA/m. The OMP of Sm(CoFeCuZr)$_z$ magnets is commonly evaluated by summing H_{cj} (in kA/m) and $(BH)_{max}$ (in kJ/m^3), with a target value of 2640. Achieving this benchmark would enable the development of a truly high-performance 2:17-type Sm−Co sintered permanent magnet.

Since the 1960s, extensive studies have been conducted to enhance the $(BH)_{max}$ and H_{cj} of 2:17-type Sm−Co magnets. Among various approaches, composition optimisation has been crucial in enhancing the magnetic properties. Studies indicate that increasing Fe content or decreasing Cu content effectively enhances remanence B_r and $(BH)_{max}$. Consequently, Sm(CoFeCuZr)$_z$ magnets with high-Fe and low-Cu compositions have become a key focus for achieving high $(BH)_{max}$ [6,7]. Currently, most high-$(BH)_{max}$ Sm–Co magnets contain 18−25 wt.% Fe and 3−5 wt.% Cu. While magnets with higher Fe content can achieve B_r values up to 1.2 T, they tend to exhibit a noticeable Cu-lean phenomenon along the grain boundary (GB), which disrupts the formation of the nearby cellular structure, severely compromising coercivity [8,9]. To counter this effect, reducing Fe content or increasing Cu content is a viable strategy. This strategy can considerably improve coercivity, lower the coercivity temperature coefficient and enhance the high-temperature magnetic performance of Sm−Co magnets. However, Sm−Co magnets with low-Fe and high-Cu contents exhibit relatively low $(BH)_{max}$, making them unsuitable for high-temperature applications [10,11]. Due to the distinct magnetic properties of high-Fe, low-Cu and low-Fe, high-Cu Sm(CoFeCuZr)$_z$ magnets, a single-alloy approach cannot fully meet the requirements for achieving optimal OMP. To address this challenge, this study adopts a dual-alloy sintering process, inspired by its successful application in preparing Nd−Fe−B sintered magnets [12], and develops a new dual-alloy approach that combines high-Fe, low-Cu Sm(CoFeCuZr)$_z$ alloy with low-Fe, high-Cu Sm(CoFeCuZr)$_z$ alloy in controlled proportions to leverage the advantages of both compositions, thereby producing high-performance dual-alloy magnets.

Therefore, in this study, sintered magnets were prepared using two types of Sm(CoFeCuZr)$_z$ alloys with different compositions, high-Fe, low-Cu and low-Fe, high-Cu, by mixing powders in varying proportions, followed by sintering and heat treatment. Specifically, the nominal composition of $Sm(Co_{0.645}Fe_{0.28}Cu_{0.055}Zr_{0.02})_{7.85}$ (20.01 wt.% Fe and 4.47 wt.% Cu) was chosen as the Type A alloy (high-Fe, low-Cu), while $Sm(Co_{0.725}Fe_{0.15}Cu_{0.1}Zr_{0.025})_{7.6}$ (10.53 wt.% Fe and 7.99 wt.% Cu) was designated as the Type B alloy (low-Fe, high-Cu). After processing, these alloys form the Type A magnet and Type B magnet, respectively.

Furthermore, to further refine the microstructure and improve the magnetic properties of Sm(CoFeCuZr)$_z$ magnets, we employed a new preparation method developed in previous study [13−15]. This method integrates key technologies such as strip-casting (SC), hydrogen decrepitation (HD), jet milling (JM) and solid solution processing to fabricate the magnets. The objective of this study is to develop high-performance Sm−Co sintered magnets by combining the dual-alloy approach with this new preparation technique, thereby improving overall magnetic properties. Specifically, we aim to achieve dual-alloy magnets with a $(BH)_{max}$ exceeding 240 kJ/m^3 and an H_{cj} exceeding 2400 kA/m. In addition, this study systematically investigates the entire preparation process for high-performance Sm(CoFeCuZr)$_z$ magnets, clarifies the magnetic hardening mechanism during magnetisation reversal, and provides both theoretical insights and process guidance for the development of high-grade commercial magnets, ultimately expanding the application scope of Sm−Co permanent magnets.

2 Experimental

The magnets investigated in this study were fabricated using powder metallurgy. The process involved several key steps: alloy melting, SC, HD, JM, powder mixing, alignment, compacting, sintering and heat treatment. Specifically, SC flakes with nominal compositions of Type A and B magnets were produced using induction melting and a single-roller SC process at a rotating speed of 0.5 m/s in an argon atmosphere. An additional 5 wt.% of Sm was added to compensate for losses during melting and SC. The SC process is shown in Fig. S1 (in Supporting Materials (SM)). Following this, the SC flakes were crushed into powders using HD and JM in sequence. By adjusting the JM speed, the average particle sizes of Type A and B magnet powders were 3.53 and 2.01 μm, respectively. The morphology of the JM powders is shown in Fig. S2 in SM. After mixing the JM powders of Type A and B magnets in various proportions based on the total mass of the magnet, the blended powders were aligned and pressed under a magnetic field of 1.6×10^6 A/m, followed by isostatic compaction at a pressure of 250 MPa for 120 s. To investigate the magnetic properties of magnets with different powder mixing ratios, a process optimisation was performed to determine the ideal sintering and solid solution temperatures for the green bodies. The powder mixture was sintered to be 1200−1220 °C for 1 h, while the solid solution treatment was conducted at 1155−1180 °C for 5 h under an argon atmosphere, followed by rapid air cooling to room temperature (approximately 20 °C). Finally, the ageing treatment was performed at 810 °C for 40 h, after which the temperature was gradually reduced to 420 °C at a rate of 0.4 °C/min. The material was then held at 420 °C for 10 h before cooling to room temperature.

The magnetic properties of the samples were measured using an ultra-high-temperature measurement system (NIM−500C) developed by the National Institute of Metrology of China over a temperature range of 100−300 °C. Room temperature magnetic properties and the initial magnetisation curve were tested with a pulsed field magnetometer system (PFM14). The microstructures and elemental distribution of the samples were examined using scanning electron microscopy (SEM, FEI Nova Nano 200) and transmission electron microscopy (TEM, JEM−2100F). The backscattered electron (BSE) images and surface elemental distribution were analysed with an electron probe micro-analyzer (EPMA) equipped with a wavelength-dispersive X-ray detector (JEOL JXA800). The magnetic domain and the process of reverse magnetisation were studied using a magneto-optical Kerr effect (MOKE) microscope (BH−786IP−PK NEOARK CORP).

3 Results and discussion

3.1 Magnetic property

Figure 1(a) presents the demagnetisation curves and Table 1 lists the magnetic parameters of the final magnets [(100−x)wt.%A+$x$wt.%B] with x=0, 20, 30, 35, 40, 50 and 100. The results show considerable variations in the magnetic properties of Sm(CoFeCuZr)$_z$ magnets with varying compositions. The magnet A, with high-Fe and low-Cu composition, exhibits a higher B_r (1.18 T) but a lower H_{cj} (1384 kA/m). In contrast, the magnet B, with low-Fe and high-Cu composition, has a lower B_r (1.03 T) but considerably higher H_{cj} (3406.4 kA/m). Furthermore, after sintering with the mixed powders, the B_r of the dual-alloy magnet decreases as the mixing amount (x) increases. This reduction is attributed to the addition of the alloy B (low-Fe and high-Cu composition), which lowers the overall Fe content in the magnet. However, compared with the magnet A, the dual-alloy magnets demonstrate considerably higher coercivity. Notably, the magnetic properties improve substantially when x=35 and 40, yielding dual-alloy magnets with $(BH)_{max}$ > 240 kJ/m^3 and H_{cj} > 2400 kA/m. The OMP values reach 2939.2 and 2973.68, respectively, meeting the magnetic performance criteria for high-performance Sm(CoFeCuZr)$_z$ magnets. Morover, since the magnet exhibits better squareness at x=35, this composition is considered to provide the best overall performance.

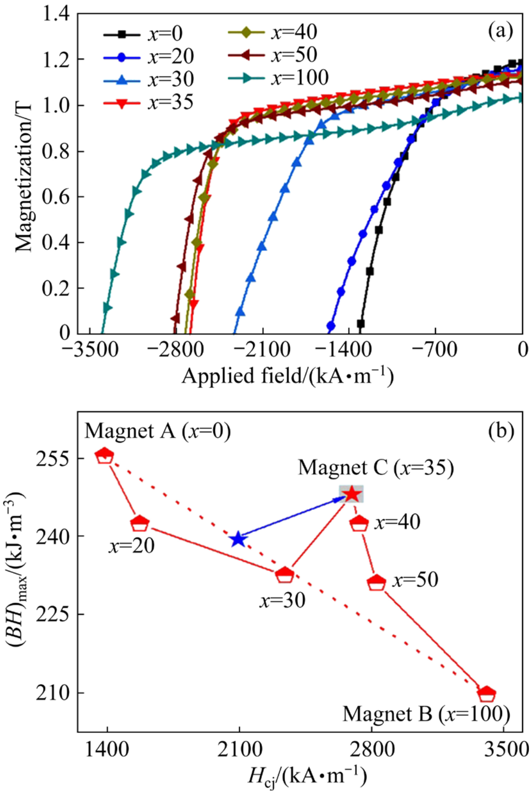

Fig. 1 (a) Demagnetization curves for magnets; (b) Comparison of magnetic properties (The blue star represents the magnetic properties derived by combining the H_{cj} and $(BH)_{max}$ of the magnets A and B at a powder mixing ratio of 65:35, while the red star represents the magnetic properties of the magnet C)

Table 1 Magnetic properties of [(100−x)wt.%A+$x$wt.%B] sintered magnets

Magnet	B_r/T	H_{cj}/ (kA·m^{-1})	$(BH)_{max}$/ (kJ·m^{-3})	(H_k/H_{cj})/ %	OMP
x=0	1.18	1384.0	255.52	64.1	1639.52
x=20	1.16	1569.6	242.48	44.5	1812.08
x=30	1.14	2337.6	232.56	44.9	2570.16
x=35	1.13	2691.2	248.00	64.5	2939.20
x=40	1.12	2731.2	242.48	58.3	2973.68
x=50	1.11	2822.4	231.12	49.8	3053.52
x=100	1.03	3406.4	209.68	26.0	3616.08

Figure 1(b) compares magnetic characteristics of the magnet A (x=0), the magnet B (x=100), the magnet C (x=35) and other hybrid magnets. The results show that compared with the expected composite properties, the magnet C exhibits significantly improved H_{cj} and $(BH)_{max}$. Notably, the coercivity of the magnet C increases from 2092 to 2691.2 kA/m, with a 28.6% enhancement, while its OMP remains excellent.

3.2 Microstructure and element distribution

A considerable improvement in the OMP is attributed to structural modifications introduced by the dual-alloy process. To analyse these effects, the microstructures and elemental distributions of the magnets A, B and C are examined, as shown in Fig. 2. The line distribution of Cu across GBs in the magnet A is shown in Fig. S3 in SM. The results indicate that the magnet A develops a well-defined and clear GB structure, with a relatively uniform distribution of Sm, Fe and Zr. However, a minor Cu-lean phenomenon is observed at certain GB regions, as highlighted by the white line in the Cu elemental distribution shown in Fig. 2(a). In the magnet B, the elemental distribution within the grains remains relatively uniform, but the Cu elemental distribution along the GBs differ notably from that within the grains, exhibiting a clear Cu-lean phenomenon, as indicated by the blue arrow in Fig. 2(c). The pronounced Cu-lean phenomenon leads to low squareness ratio of H_k/H_{cj} (26.0%) for the magnet B, along with a reduced knee point (H_k), both of which limit the OMP of the magnet B.

In contrast, the elemental distribution in the magnet C, as shown in Fig. 2(b), reveals no observable Cu-lean phenomenon along GBs at the microscale. Instead, all elements are uniformly distributed. According to the EPMA results, the dual-alloy process promotes uniform elemental distribution of the various components within both the grains and GBs of the magnet, mitigates GB defects and ultimately leads to a homogeneous microstructure. A uniform microstructure enhances the coercivity and squareness of the magnet, thereby improving its OMP [10,16].

To further investigate the improvement in magnetic properties at the nanoscale, the microstructure and microchemistry of the magnets A and C

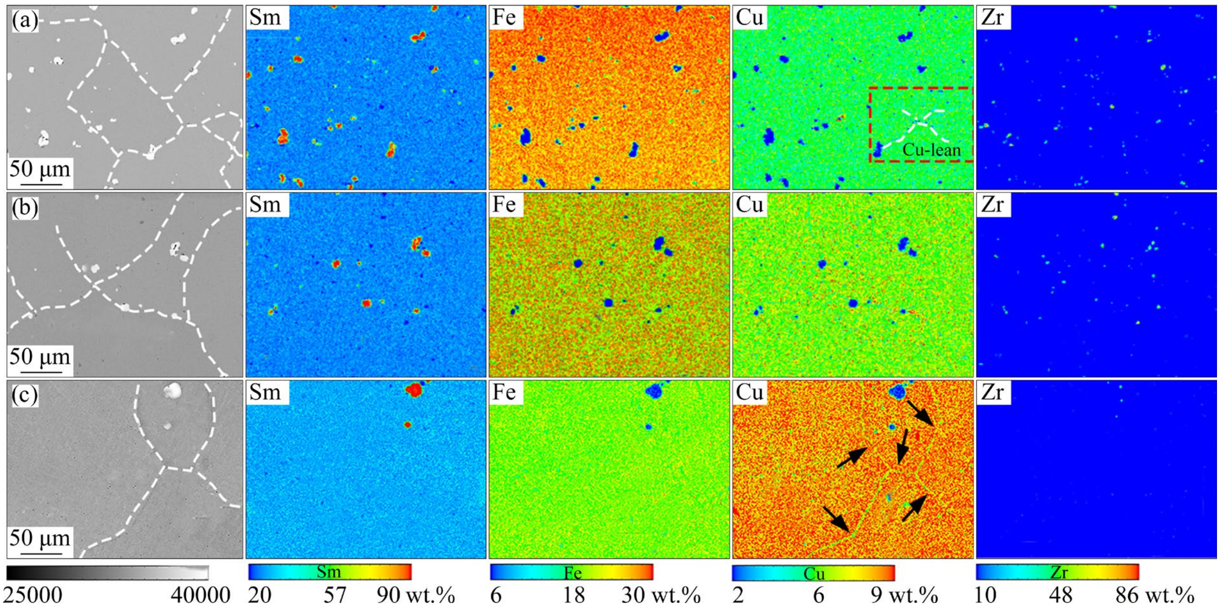

Fig. 2 BSE images and EPMA element distribution: (a) Magnet A; (b) Magnet C; (c) Magnet B

are examined. Figure 3 shows the TEM results of the magnets A and C along the [001]-2:17R zone-axis, and the TEM−EDS results for the selected cell boundary phases and cell phases in Fig. 3 are provided in Table 2. The results indicate that both magnets exhibit typical nanocellular structures, with the average cellular size being ~107.2 and ~99.9 nm, as shown in Figs. 3(a, c), respectively. Furthermore, the magnet A exhibits uneven cellular size distribution, with some individual cellular structures developing abnormally, reaching a maximum size of ~243.5 nm, while the cellular structures in the magnet C are relatively small and uniform. Figures 3(b, d) show the bright field TEM images of the GBs in the two magnets, respectively. It can be observed that distinct GBs are present in the magnet C, with complete cellular structures surrounding them. In contrast, some GBs in the magnet A exhibit incomplete structures, as indicated by red area in Fig. 3(b). The Cu-lean phenomenon along the GBs in the A magnet (shown in Fig. 2(a)) leads to the formation of incomplete cellular structures around these boundaries. This also suggests that the dual-alloy magnet contains a higher volume fraction of the cell boundary phase, which contributes to a significant increase in coercivity [17].

Furthermore, the results in Table 2 show that the composition distribution of the cell boundary and cell phases in different regions of the magnet A varies considerably. In the magnet A, the Cu concentration at Points 2 and 4 (Fig. 3(a)) of the cell boundary phases is 32.4 and 20.1 at.%, respectively. Additionally, these points still contain a higher Fe concentration, suggesting that the spinodal decomposition is incomplete and uneven [18−20]. However, during the sintering process of the dual-alloy mixed powder, the Cu content is indirectly increased. As the Cu element fully diffuses into the grain and GB, the Cu concentration in both the cell boundary and cell phases is considerably enhanced. Moreover, the Cu element is uniformly distributed in both the cell boundary phase and cell phase across various regions. For instance, the Cu concentration at Points 6 and 8 of the cell boundary phases is 35.2 and 36.1 at.%, respectively. Additionally, the Cu concentration at Points 5 and 7 (Fig. 3(c)) of the cell phases is 5.2 and 4.9 at.%, respectively.

Additionally, to compare the differences in phase content between the two magnets, the Rietveld fitting of the XRD patterns for both magnets is

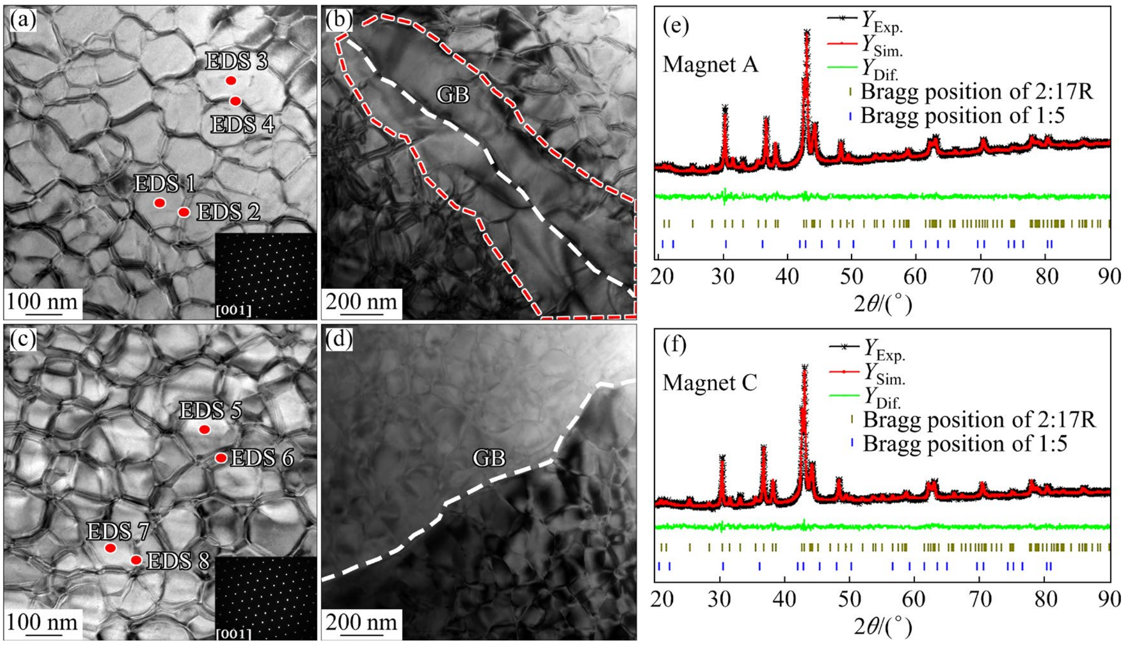

Fig. 3 TEM images of final magnets along [001]-2:17R zone-axis, showing bright field TEM images of cellular structure and grain boundaries (GBs) of (a, b) magnet A and (c, d) magnet C (The insets in (a) and (c) show the corresponding selected area electron diffraction patterns); Rietveld refinement of step-scanned XRD profiles for magnets A (e) and C (f) (The black line represents the experimental XRD pattern (Exp.), the red line represents the simulated XRD pattern (Sim.), the green line shows the difference between the experimental and simulated patterns (Dif.), and the vertical lines indicate the characteristic Bragg positions of the corresponding phases)

Table 2 TEM–EDS results of selected cell boundary and cell phases in Fig. 3 (at.%)

Magnet	Region	Sm	Co	Fe	Cu	Zr
A	1	11.2	56.7	25.2	5.6	1.3
	2	15.4	34.3	16.2	32.4	1.7
	3	12.9	57.7	24.5	2.9	2.0
	4	16.1	46.3	15.7	20.1	1.8
C	5	11.5	56.4	25.8	5.2	1.1
	6	16.3	33.2	14.1	35.2	1.2
	7	11.9	55.8	26.2	4.9	1.2
	8	16.8	33.1	12.7	36.1	1.3

shown in Fig. 3(e), revealing the phase fractions. The mass fractions of different phases determined by Rietveld analysis, along with the *R* factors, are listed in Table 3. It can be observed that both magnets are primarily composed of a 1:5 phase and a 2:17R phase [21]. However, the phase content differs, as indicated in Table 3. The A magnet contains 7.66 wt.% of the 1:5 phase and 92.34 wt.% of the 2:17R phase, while the C magnet contains 10.47 wt.% of the 1:5 phase and 89.53 wt.% of the 2:17R phase. Based on the element distribution at the micrometre scale (Fig. 2), it can be concluded that the dual-alloy magnet has a higher Cu content, with a larger Cu gradient between the cell boundary phase and the intracellular phase (Fig. 3 and Table 2) [22]. Additionally, the relatively high content of the 1:5 phase in the dual-alloy magnet contributes to an increased pinning field strength, which considerably enhances its coercivity [23,24].

Table 3 Mass fractions of different phases evaluated by Rietveld analysis and *R* factors for magnet powders in Fig. 3(e)

Magnet	Mass fraction/%		*R* factor		
	1:5	2:17R	R_p	R_{wp}	R_{exp}
A	7.66	92.34	1.15	2.34	1.30
C	10.47	89.53	1.22	2.51	1.45

3.3 Coercivity mechanism

The initial magnetisation curves of the three magnets are shown in Fig. 4(a). All three curves exhibit a typical ‘S’ shape, indicating that as the external field is applied from 0 T, the magnetisation gradually increases. However, once the external field exceeds a certain threshold, the magnetisation rapidly increases to saturation. This behaviour suggests that the coercivity mechanism of all three magnets is dominated by domain wall pinning. Additionally, the results indicate that the saturation magnetisation (M_s) for the three magnets are 1.24, 1.14 and 1.2 T, respectively. This suggests that the dual-alloy mixed powder sintering process has diluted and reduced the Fe concentration in the magnets, leading to a decline in M_s and B_r [25].

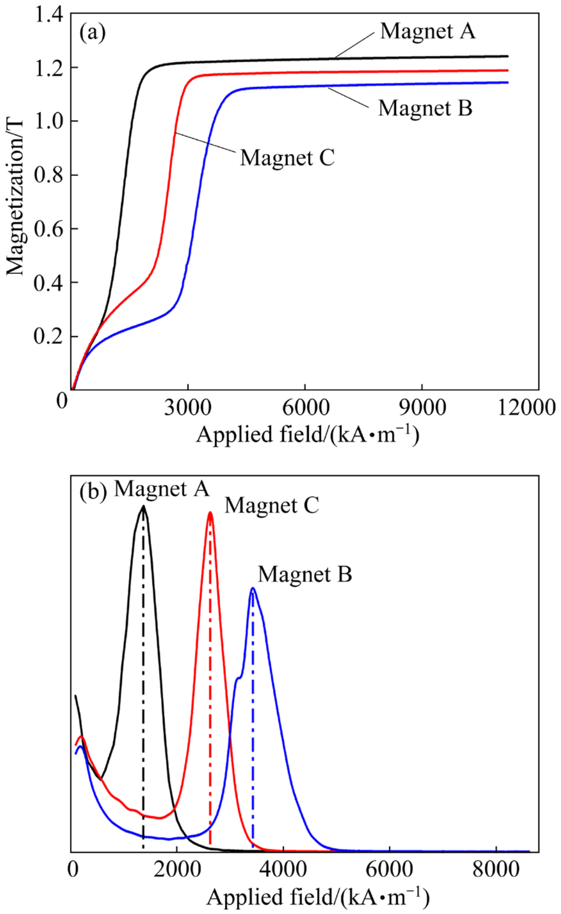

Fig. 4 (a) Initial magnetisation curves of magnets A, B and C and (b) first derivative curves of initial magnetisation curves

Furthermore, the first derivative curves of the initial magnetisation curves of the magnets are shown in Fig. 4(b). These curves indicate that the magnets A, B and C have maximum pinning fields of 1384, 3408 and 2696 kA/m, respectively. These values are in close agreement with the coercivity values obtained from the demagnetisation curves (Fig. 1). The findings demonstrate that when dual-alloy magnet composition is 65wt.%A+35wt.%B, the coercivity mechanism remains unchanged, maintaining a domain wall pinning behaviour. However, the pinning field strength is considerably improved by 94.8% compared to the single-alloy magnet A.

3.4 Magnetic domain structure and magnetisation reversal process

To better understand the relationship between magnetic properties and the microscopic domain structure of the magnets A, B and C, magnetic domain patterns are observed using MOKE in a thermally demagnetised state, as shown in Fig. 5. Detailed information on the magnetic domains is provided in Table 4. The observation surface is oriented perpendicular to the *c*-axis of the magnet.

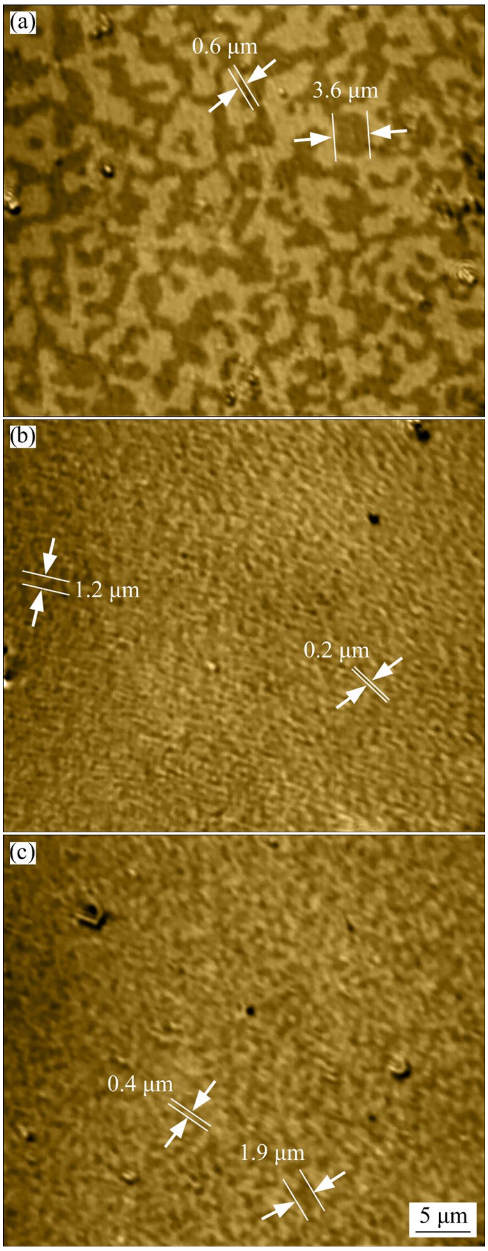

Fig. 5 MOKE results of sintered magnets, with observation surface perpendicular to *c*-axis: (a) Magnet A; (b) Magnet B; (c) Magnet C

Table 4 Magnetic domain widths of magnets A, B and C

Magnet	Domain width range/μm	Average domain width/μm
A	0.6−3.6	1.6
B	0.2−1.2	0.6
C	0.4−1.9	1.1

Figure 5 shows that all three magnets exhibit ‘maze-like’ domain patterns, although their domain widths vary significantly. The domain width of the magnet A (Fig. 5(a)) ranges from 0.6 to 3.6 μm, with an average domain width of 1.6 μm. In contrast, the B magnet domain has a smaller and more uniform domain width, ranging from 0.2 to 1.2 μm (Fig. 5(b)), with an average domain width of 0.6 μm. The magnet C (Fig. 5(c)) exhibits a domain width of 0.4−1.9 μm, with an average domain width of approximately 1.1 μm. Notably, the magnet A, with the lowest coercivity, exhibits the highest domain width, while the magnet B, with ultra-high coercivity, has the smallest domain width. These results suggest that when sintered magnets are prepared using the dual-alloy process, the average domain width decreases as coercivity increases. This inverse relationship between domain width and coercivity aligns with findings reported in the literature [25−27].

To further clarify the demagnetisation mechanism and its correlation with the enhancement of coercivity and squareness, the magnetisation reversal process of the magnets A, B and C is observed using MOKE, as shown in Fig. 6. Before MOKE analysis, all magnets are first magnetised to a saturation state using an external magnetic field of 10 T. Under a maximum external field of 1.5 T, all three magnets exhibit a single-domain state. As the external magnetic field decreases to 0.9 T, reverse domains with dark contrast appear at certain GBs of the magnet A, indicating the onset of domain reversal (as indicated by the white arrows in Fig. 6). As the applied external field further decreases to 0 T, the magnet A exhibits distinct reversal domains at GBs (as indicated by the red arrows in Fig. 6), while a few black reversal domains begin to emerge at individual GBs in the magnet B. When the applied magnetic field is reduced to −0.4 T, a few ‘cloud-like’ reverse domains appear within the grains of the magnet A, while previously formed reversal domains at the GBs begin to expand into the grain interior. At this stage, reverse domains also start to appear at the GBs of the

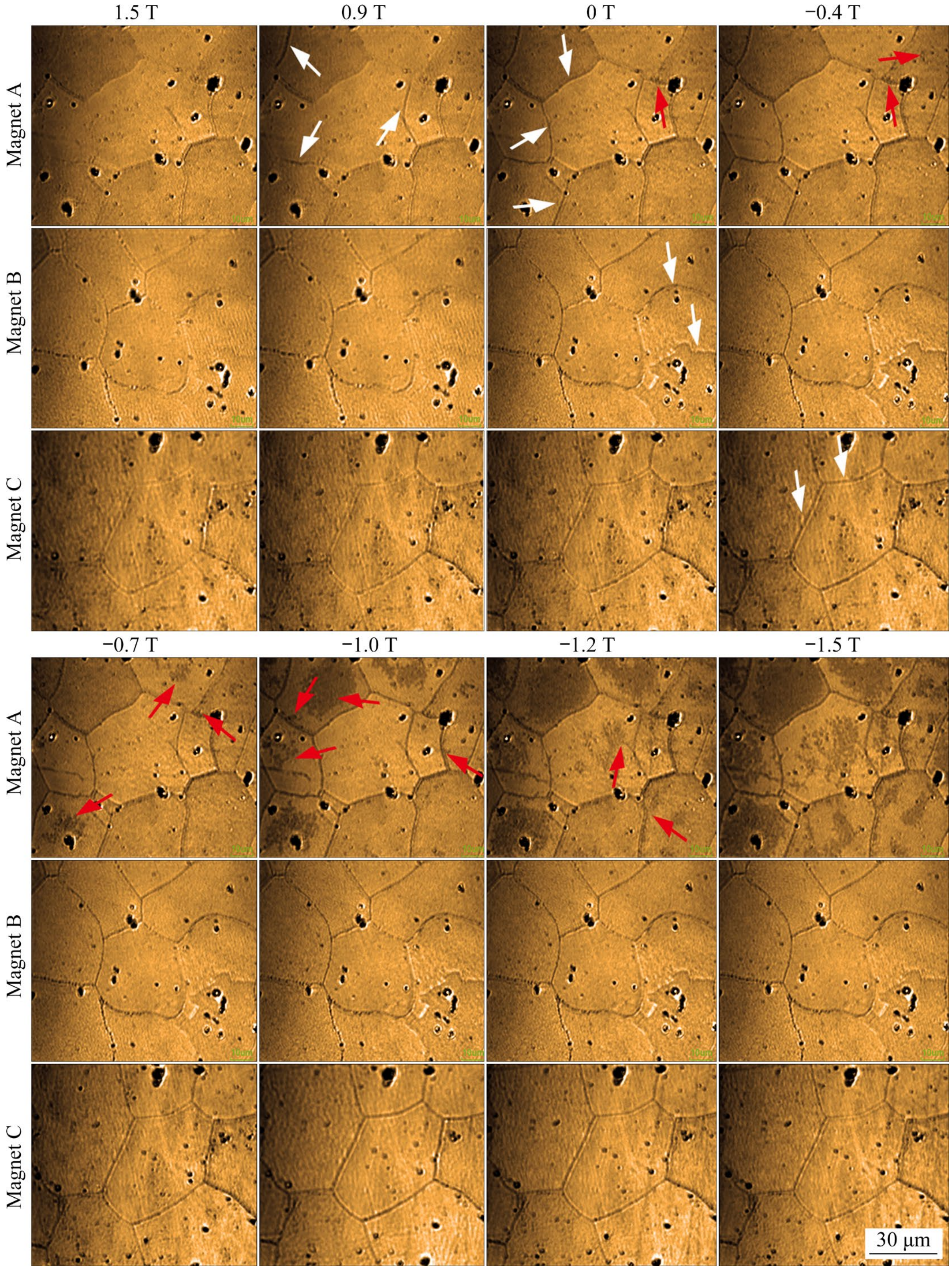

Fig. 6 Magnetic domain evolution of magnets A, B and C during demagnetisation process

magnet C. As the reverse magnetic field decreases to −0.7 T and below, the 'cloud-like' reverse domains in the magnet A expand further into the grain interior, leading to an increased magnetisation reversal. In contrast, for the magnets B and C, even at an applied external magnetic field of −1.5 T, reverse domains remain confined to the GBs, without expansion into the grains. These results indicate that the C magnet, prepared using the dual-alloy process, achieves a uniform elemental distribution and a complete cellular structure near the GBs, considerably enhancing the pinning field [28]. Therefore, the GBs in the magnet C exhibit a significant pinning effect, preventing the expansion of reverse domains, even under large external fields.

3.5 High-temperature magnetic properties

The demagnetisation curves of the magnet C at temperatures of 20, 100, 150, 200 and 300 °C are shown in Fig. 7, with the corresponding magnetic performance parameters listed in Table 5. The results indicate that as the test temperature increases, H_{cj}, B_r and $(BH)_{max}$ of the magnet C all decrease. At 300 °C, the magnet exhibits the following magnetic properties: B_r=1.01 T, H_{cj}=1066.4 kA/m and $(BH)_{max}$=184.24 kJ/m^3. Calculations reveal that the remanence temperature coefficient ($\alpha_{20-300\,°C}$) is −0.20% °C^{-1}. Based on these high-temperature performance results, the dual-alloy magnet demonstrates strong thermal stability and remains suitable for applications at temperatures up to 300 °C [29].

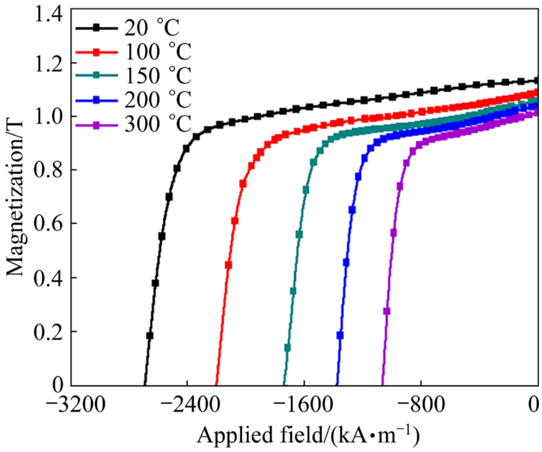

Fig. 7 Demagnetization curves of magnet C (20−300 °C)

Table 5 Magnetic properties of magnet C (20−300 °C)

Test temperature/°C	B_r/T	H_{cj}/(kA·m^{-1})	$(BH)_{max}$/(kJ·m^{-3})	H_k/(kA·m^{-1})
20	1.13	2691.2	248.00	1735.2
100	1.09	2200.0	222.72	1383.2
150	1.06	1740.8	204.48	1131.2
200	1.04	1375.2	195.68	924.8
300	1.01	1066.4	184.24	734.4

3.6 Effect of preparation process on magnetic properties and microstructure

Based on the aforementioned findings, the magnet C prepared using the dual-alloy process exhibits the optimal OMP when x=35. At this composition, $(BH)_{max}$ and H_{cj} exceed 240 kJ/m^3 and 2400 kA/m, respectively, while the OMP reaches 2939.2. The calculated composition of the C magnet is $Sm_{25}Co_{50}Fe_{17}Cu_6Zr_2$ (wt.%). For comparison, a single-alloy process is used to prepare a magnet with the same nominal composition as the magnet C. The demagnetisation curves and magnetic properties of this magnet are presented in Fig. 8 and Table 6, respectively. The results indicate that while the B_r values of two magnets prepared using different processes are not significantly different, notable differences are observed in H_{cj} and H_k/H_{cj}, which consequently influence the $(BH)_{max}$. Notably, the coercivity, $(BH)_{max}$ and squareness of magnets produced by the single-alloy process are lower compared to those made using dual-alloy process. These results highlights the clear advantage of the dual-alloy process for achieving high-performance magnets over the single-alloy process.

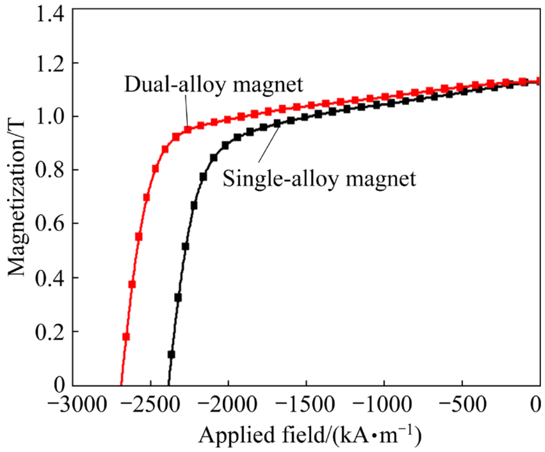

Fig. 8 Demagnetization curves of final magnets obtained through different preparation processes

To further examine these differences, BSE morphology and EPMA elemental analysis were performed on both magnets, with results shown in Fig. 9. The white dashed lines indicate GBs. Both magnets exhibit well-developed and distinct GBs. However, the magnet produced by the single-alloy process shows a pronounced Cu-lean phenomenon at the GBs, as indicated by the black arrow in the Cu elemental distribution map (Fig. 9(a)). In contrast, the Cu elemental distribution within the grains remains uniform. Conversely, for the dual-alloy magnet, no considerable Cu-lean phenomenon is observed at the GBs, with Cu distributing uniformly within the grains (Fig. 9(b)). Previous studies [28−31] have shown that Cu depletion at the GBs can lead to an uneven elemental distribution around the GBs, influencing the formation of the cellular structure and weaking the pinning effect at the GBs, thereby resulting in decreased coercivity and

Table 6 Magnetic properties of final magnets obtained using different preparation processes

Magnet	B_r/T	H_{cj}/(kA·m^{-1})	$(BH)_{max}$/(kJ·m^{-3})	H_k/(kA·m^{-1})	(H_k/H_{cj})/%	OMP
Single-alloy	1.13	2388.0	239.04	1405.6	54.4	2627.04
Dual-alloy	1.13	2691.2	248.00	1735.2	64.5	2939.20

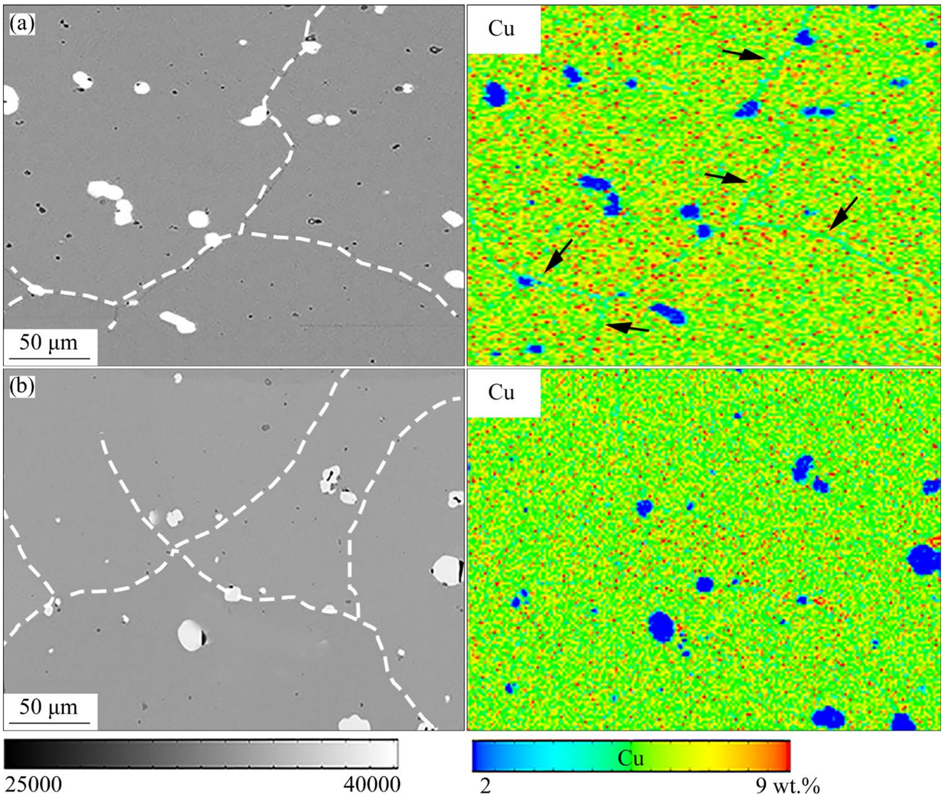

Fig. 9 BSE images and EPMA results: (a) Single-alloy magnet; (b) Dual-alloy magnet

squareness. Based on these findings, we can conclude that the significant Cu-lean phenomenon observed at GBs in single-alloy magnets restricts improvements in squareness and coercivity [30,31], resulting in lower OMPs compared with dual-alloy magnets. Therefore, the preparation process plays a crucial role in determining the microstructure and magnetic properties of a magnet.

4 Conclusions

(1) As the proportion of low-iron, high-copper alloy powder increases, the dual-alloy magnet develops a uniform microstructure with a homogeneous composition at the micrometre scale, which promotes the formation of small, uniform nanoscale cellular structures.

(2) A complete cellular structure is formed near the GBs of the dual-alloy magnets, significantly improving the pinning strength and enhancing the coercivity. When x=35 and 40, coercivity increases substantially, yielding dual-alloy magnets with $(BH)_{max} > 240$ kJ/m^3 and $H_{cj} > 2400$ kA/m. The OMP values reach as high as 2939.2 and 2973.68, respectively.

(3) Compared with the single-alloy magnets, the dual-alloy magnets exhibit a more uniform Cu elemental distribution, with no notable Cu-lean phenomenon observed at the GBs. This homogeneous microstructure contributes to enhanced magnetic properties, particularly the formation of complete nanocellular structures, which are essential for achieving high-performance 2:17-type Sm−Co magnets.

CRediT authorship contribution statement

Jian-jun YANG: Conceptualization, Data curation, Investigation, Writing – Original draft; **Dong-tao ZHANG:** Conceptualization, Supervision, Funding acquisition, Writing − Review & editing; **Yu-qing LI:** Formal analysis, Validation; **Zan LONG:** Methodology, Investigation; **Cheng-zhen MENG:** Methodology,

Investigation; **Wei-qiang LIU:** Formal analysis, Validation; **Ming YUE:** Project administration, Supervision, Funding acquisition.

Declaration of competing interest

The authors declare that they have no known competing financial interests or personal relationships that could have appeared to influence the work reported in this paper.

Acknowledgments

This work was supported by the National Key Research and Development Program for Young Scientists, China (No. 2023YFB3508400), the National Natural Science Foundation of China (Nos. 51871005, 51931007), the Key Program of Science and Technology Development Project of Beijing Municipal Education Commission of China (No. KZ202010005009), and the Program of Top Disciplines Construction in Beijing, China (No. PXM2019_014204_500031).

Supporting Materials

Supporting Materials in this paper can be found at: https://tnmsc.csu.edu.cn/download/17-p0917-2024-0966-Supporting_Materials.pdf.

References

[1] LI Xiao-qiang, LI Li, HU Ke, CHEN Zhi-cheng, QU Sheng-guan, YANG Chao. Microstructure and magnetic properties of anisotropic Nd−Fe−B magnets prepared by spark plasma sintering and hot deformation [J]. Transactions of Nonferrous Metals Society of China, 2014, 24(10): 3142−3151.

[2] LIU Bing-jie, WANG Hui, XU Hao, LIU Jing-hua, JIANG Cheng-bao. Atomic-scale transition zones determined coercivity in samarium−cobalt based permanent magnets [J]. Advanced Functional Materials, 2023, 33(50): 2304711.

[3] DONG C H, WU H C, ZHOU B, SUN Y L, DING Y, YAN A R. Effects of 1:5H-type Cu-rich phase around grain boundary on cell boundary phase and squareness of the demagnetization curve in sintered Sm_2Co_{17}-type magnets [J]. Journal of Magnetism and Magnetic Materials, 2024, 599: 172117.

[4] TENG Yuan, LI Yu-qing, XU Xiao-chang, YUE Ming, LIU Wei-qiang, ZHANG Dong-tao, ZHANG Hong-guo, LU Qing-mei, XIA Wei-xing. Microstructure evolution of hot-deformed SmCo-based nanocomposites induced by thermo-mechanical processing [J]. Journal of Materials Science & Technology. 2023, 138:193−202.

[5] WANG Chao, ZHU Ming-gang. Overview of composition and technique process study on 2:17-type Sm−Co high-temperature permanent magnet [J]. Rare Metals, 2021, 40(4): 790−798.

[6] TANG W, ZHANG Y, HADJIPANAYIS G C. Microstructure and magnetic properties of $Sm(Co_{bal.}Fe_xCu_{0.1282}Zr_{0.02})_7$ magnets with Fe substitution [J]. Journal of Magnetism and Magnetic Materials, 2000, 221: 268−272.

[7] XI Long-long, ZHANG Tian-li, HU Ming-yao, LIU Zi-heng, KANG Da-zhuang, ZHAO Ming-jing, ZUO Shu-lan, HE Yang-kun, JIANG Cheng-bao. High-remanence Fe-rich 2:17-type Sm−Co sintered magnets mediated via multiscale microstructure [J]. Advanced Engineering Materials, 2024, 26(4): 2301591.

[8] YANG Jian-jun, ZHANG Dong-tao, XIE Zhi-hong, SHANG Zhi-feng, LI Yu-qing, LIU Wei-qiang, YUE Ming. Tremendous enhancement of magnetic performance for $Sm(CoFeCuZr)_z$ magnet based on multiscale copper redistribution [J]. Journal of Rare Earths, 2022, 40(10): 1592−1597.

[9] SONG Xin, MA Tian-yu, ZHOU Xiang-long, YE Fan, YUAN Tao, WANG Jing-dong, YUR Ming, LIU Feng, REN Xiao-bing. Atomic scale understanding of the defects process in concurrent recrystallization and precipitation of Sm−Co−Fe−Cu−Zr alloys [J]. Acta Materialia, 2021, 202: 290−301.

[10] CAO Jun, ZHANG Tian-li, LIU Jing-hua, XU Hao, HU Ming-yao, XIA Wei, WANG Ao, WANG Hui, JIANG Cheng-bao. Grain boundary optimization induced substantial squareness enhancement and high performance in iron-rich Sm−Co−Fe−Cu−Zr magnets [J]. Journal of Materials Science & Technology, 2021, 85: 56−61.

[11] LIU Zhuang, WU Hai-chen, ZHANG Chao-yue, ZHU Chao-qun, CHEN Guo-xin, LU Huan-ming, CHEN Ren-jie, YAN A-ru. Significant effect of ordered micro-domain on cell boundary phase distribution and demagnetization curve squareness of Sm_2Co_{17}-type magnet [J]. Rare Metals, 2024, 43(4): 1724−1735.

[12] ZHANG Yi-Jie, LIU Ying-ying, DAI Yu, TAN Dun-qiang, JIANG Wei-wei, YI Zhi-qiang, WU Jian, SHENG Xiao-die, YAO Wen-jiao. Coercivity enhancement via synergetic effect of dual-alloy and grain boundary diffusion strategies in Nd−Fe−B permanent magnet [J]. Journal of Magnetism and Magnetic Materials, 2024, 589: 171561.

[13] YANG Jian-jun, ZHANG Dong-tao, ZHANG Hong-guo, LI Yu-qing, MENG Cheng-zhen, TENG Yuan, LIU Wei-qiang, YUE Ming. Combination strategy for high-performance $Sm(CoFeCuZr)_z$ sintered permanent magnet: Synergistic improvement of the preparation process [J]. Acta Materialia, 2023, 251: 118901.

[14] YANG Jian-jun, ZHANG Dong-tao, ZHANG Hong-guo, SHANG Zhi-feng, WANG Hong, MENG Cheng-zhen, LIU Wei-qiang, YUE Ming. Effect of hydrogen pressure on hydrogenation and pulverization behavior of $Sm(CoFeCuZr)_z$ ingot and strip casting flake [J]. Journal of Alloys and Compounds, 2023, 930: 167427.

[15] MENG C Z, ZHANG D T, JIA J H, YANG J J, TENG Y, ZHANG H G, LI Y Q, LIU W Q, YUE M. Effect of casting methods on magnetic properties of Sm $(CoFeCuZr)_z$ magnet [J]. AIP Advances, 2023, 13(2): 025324.

[16] SONG Kui-kui, SUN Wei, FANG Yi-kun, WANG Shuai, YU Neng-jun, ZHANG Mei-ling, ZHU Ming-gang, LI Wei. Optimization of microstructures and magnetic properties of $Sm(Co_{bal}Fe_{0.227}Cu_{0.07}Zr_{0.023})_{7.6}$ magnets by sintering treatment [J]. Journal of Rare Earths, 2019, 37(2): 171−177.

[17] ZHANG Chao-yue, LIU Zhuang, WANG Guang-qing, YAN Guang-hui, CHEN Ren-jie, LEE Don, YAN A-ru. Effect of residual hydrogen on microstructure and magnetic properties of $Sm(Co_{0.647}Fe_{0.28}Cu_{0.053}Zr_{0.02})_{7.84}$ magnets [J]. Journal of Alloys and Compounds, 2019, 795: 513−518.

[18] SEPEHRI-AMIN H, THIELSH J, FISCHBACHER J, OHKUBO T, SCHREFL T, GUTFLEISCH O, HONO K. Correlation of microchemistry of cell boundary phase and interface structure to the coercivity of $Sm(Co_{0.784}Fe_{0.100}Cu_{0.088}Zr_{0.028})_{7.19}$ sintered magnets [J]. Acta Materialia, 2017, 126: 1−10.

[19] LI Qiang-feng, WANG Chao, WANG Lei, BI Yi-fei, FANG Yi-kun, ZHANG Yue, ZHU Ming-gang, LI Wei. Unveiling the homogenization microstructure evolution and its effect on cellular structure for Fe-rich Sm−Co−Fe−Cu−Zr magnets [J]. Journal of Materials Science & Technology, 2024, 194: 142−150.

[20] XIONG X Y, OHKUBO T, KOYAMA T, OHASHI K, TAWARA Y, HONO K. The microstructure of sintered $Sm(Co_{0.72}Fe_{0.20}Cu_{0.055}Zr_{0.025})_{7.5}$ permanent magnet studied by atom probe [J]. Acta Materialia, 2004, 52: 737−748.

[21] ZHOU Xiang-long, YUAN Tao, MA Tian-yu. Shortened processing duration of high-performance Sm−Co−Fe−Cu−Zr magnets by stress-aging [J]. Journal of Materials Science & Technology, 2022, 106: 70−76.

[22] SHANG Zhi-feng, ZHANG Dong-tao, XIE Zhi-hong, WANG Yun-qiao, Haseeb Muhammad, Qiao Peng-biao, LIU Wei-qiang, YUE Ming. Effect of copper and zirconium contents on microstructure and magnetic properties of $Sm(Co,Fe,Cu,Zr)_z$ magnets with high iron content [J]. Journal of Rare Earths, 2021, 39(2): 160−166.

[23] WANG G Q, LIU Z, ZHANG C Y, YANG Q Q, WU H C, CHEN R J, YAN A R. Cellular structure regulation and coercivity enhancement induced by La_2O_3 doping in 2:17 type SmCo magnet [J]. Journal of Alloys and Compounds, 2020, 849: 156589.

[24] CHEN Han-sheng, WANG Yun-qiao, YAO Yin, QU Jiang-tao, YUN Fan, LI Yu-qing, RINGER S P, YUE Ming, ZHENG Rong-kun. Attractive-domain-wall-pinning controlled Sm−Co magnets overcome the coercivity-remanence trade-off [J]. Acta Materialia, 2019, 164: 196−206.

[25] WANG Y Q, SHANG Z F, YUE M, WU D, ZHANG D T, ZHANG H G, LIU W Q. Correlation between Fe content and z value in $Sm(Co_{bal}Fe_xCu_{0.06}Zr_{0.025})_z$ permanent magnets [J]. Journal of Magnetism and Magnetic Materials, 2019, 474: 417−423.

[26] GUTFLEISCH O, MÜLLER K H, KHLOPKOV K, WOLF M, YAN A, SCHÄFER R, GEMMING T, SCHULTZ L. Evolution of magnetic domain structures and coercivity in high-performance SmCo 2:17-type permanent magnets [J]. Acta Materialia, 2006, 54: 997−1008.

[27] ZHANG Xiang-yi, HUA Ying-xin, LI Xiao-hong. Aligning nano-scale crystals in bulk materials [J]. Science China Physics, Mechanics & Astronomy, 2025, 68: 247511.

[28] LIU Man-ying, LI Yu-qing, ZHANG Dong-tao, WU Qiong, YANG Jian-jun, ZHANG Hong-guo, ZHANG Le-le, YUE Ming. Understanding of magnetization reversal mechanism of precipitation-hardening samarium-cobalt magnets from micromagnetic simulation [J]. Applied Physics Letters, 2024, 124: 042403.

[29] KRONMÜLLER H, GOLL D. Analysis of the temperature dependence of the coercive field of Sm_2Co_{17} based magnets [J]. Scripta Materialia, 2003, 48: 833−838.

[30] SONG Xin, ZHOU Xiang-long, YUAN Tao, WANG Jing-dong, YUE Ming, MA Tian-yu. Role of nanoscale interfacial defects on magnetic properties of the 2:17-type Sm−Co permanent magnets [J]. Journal of Alloys and Compounds, 2020, 816: 152620.

[31] ZHOU Xiang-long, SONG Xin, JIA Wen-tao, XIAO An-dong, YUAN Tao, MA Tian-yu. Identifications of $SmCo_5$ and $Sm_{n+1}Co_{5n-1}$-type phases in 2:17-type Sm−Co−Fe−Cu−Zr permanent magnets [J]. Scripta Materialia, 2020, 182: 1−5.

双合金工艺制备高性能 $Sm(CoFeCuZr)_z$ 烧结永磁体的磁硬化策略

杨建军 [1,2]，张东涛 [1,3]，李玉卿 [1,3]，陇 赞 [1,3]，孟城真 [1,3]，刘卫强 [1,3]，岳 明 [1,3]

1. 北京工业大学 材料科学与工程学院 新型功能材料教育部重点实验室，北京 100124；
2. 安阳工学院 机械与航空制造工程学院，安阳 455000；
3. 北京工业大学 材料循环低碳再生全国重点实验室，北京 100124；

摘 要：为提高 $Sm(CoFeCuZr)_z$ 烧结磁体的综合磁性能，系统研究了一种将高铁低铜与低铁高铜合金粉末混合的双合金烧结工艺。结果表明，该方法能有效改善晶界贫铜现象，获得多尺度均匀的显微组织，大幅提高钉扎场强度，最终制备出最大磁能积($(BH)_{max}$)超过 240 kJ/m³、内禀矫顽力(H_{cj})超过 2400 kA/m 的高性能双合金磁体。特别是当掺入 35%(质量分数)的低铁高铜合金粉末时，获得双合金磁体的剩磁为 1.13 T，H_{cj} 为 2691.2 kA/m，$(BH)_{max}$ 为 248 kJ/m³。采用 H_{cj}(kA/m)和$(BH)_{max}$(kJ/m³)之和作为综合磁性能评价指标，其数值可达 2939.2。相较于同成分单合金工艺制备的磁体，双合金烧结工艺获得的磁体不仅元素分布更均匀，且展现出更优异的磁性能。

关键词：$Sm(CoFeCuZr)_z$ 磁体；双合金烧结工艺；磁性能；矫顽力机理；反磁化过程

(Edited by Bing YANG)